

A manifold learning approach for gesture identification from micro-Doppler radar measurements

E. Mason*, H. N. Mhaskar[†] A. Guo[‡]

Abstract

A recent paper (Neural Networks, **132** (2020), 253-268) introduces a straightforward and simple kernel based approximation for manifold learning that does not require the knowledge of anything about the manifold, except for its dimension. In this paper, we examine the pointwise error in approximation using least squares optimization based on this kernel, in particular, how the error depends upon the data characteristics and deteriorates as one goes away from the training data. The theory is presented with an abstract localized kernel, which can utilize any prior knowledge about the data being located on an unknown sub-manifold of a known manifold.

We demonstrate the performance of our approach using a publicly available micro-Doppler data set investigating the use of different pre-processing measures, kernels, and manifold dimension. Specifically, it is shown that the Gaussian kernel introduced in the above mentioned paper leads to a near-competitive performance to deep neural networks, and offers significant improvements in speed and memory requirements. Similarly, a kernel based on treating the feature space as a submanifold of the Grassman manifold outperforms conventional hand-crafted features. To demonstrate the fact that our methods are agnostic to the domain knowledge, we examine the classification problem in a simple video data set.

Keywords: Machine Learning, Kernel Methods, Micro-Doppler Radar Gesture Recognition

1 Introduction

Identification of hand gestures is a subject of increasing research attention in the area of human-computer interaction, see for example, [2, 27] for recent reviews. Applications include convenient device control, infection prevention in clinical settings, safer and quicker accessibility of features in automotive, and, in a more general sense, detection of unmanned aerial vehicles. In contrast to the commonly used hand gesture signal acquisition approaches such as camera, infra-red sensors, and ultrasonic sensors, radar sensors are observed to yield a higher performance in adverse lighting conditions and complex background. Among the common types of waveforms used by miniature radar sensors - continuous (CW), pulse, and frequency modulated continuous waveform (FMCW)- the FMCW radars allows a simultaneous estimation of the range and the Doppler signatures. Many machine learning strategies are used for the classification of hand gestures, ranging from nearest neighbor and support vector machines (SVMs) to deep convolutional neural networks (CNNs) obtaining an accuracy as high as 95%. Except for deep networks, the work typically requires the extraction of hand crafted features based on domain knowledge. On the other hand, training a CNN is typically highly time consuming, and the mathematical theory of how, when, and why CNNs will produce the right output is still under development. In this paper, we demonstrate the use of manifold learning to classify hand gesture signals from FMCW data, agnostically of the fact that we are dealing with radar signals (i.e., independently of domain knowledge). Our general purpose method yields results that compare favorably with other, more sophisticated methods based on hand-crafted features involving domain knowledge and is not much worse than even CNNs.

The fundamental problem of machine learning is the following. We have (training) data of the form $\{(\mathbf{x}_j, f(\mathbf{x}_j) + \epsilon_j)\}$, where, for some integer $d \geq 1$, $\mathbf{x}_j \in \mathbb{R}^d$ are realizations of a random variable, f is an unknown real valued function, and the ϵ_j 's are realizations of a mean zero random variable. The distributions of both the random variables are not known. The problem is to approximate f with a suitable model, especially for the points which

*U.S. Naval Research Laboratory, 4555 Overlook Ave SW, Washington, DC 20375. email: eric.mason@nrl.navy.mil

[†]Institute of Mathematical Sciences, Claremont Graduate University, Claremont, CA 91711, U.S.A.. The research of HNM was supported in part by ARO grant W911NF2110218 and NSF DMS grant 2012355. email: hrushikesh.mhaskar@cgu.edu

[‡]Mathematics/Computer Science Department, Pomona College, Claremont, CA 91711. email: simingadam.guo@pomona.edu, agsmguo@gmail.com

are not in the training data. In the context of classification problems, f is the labeling function defined as follows. If there are K classes, we define

$$\chi_i(\mathbf{x}) = \begin{cases} 1, & \text{if } \mathbf{x} \text{ belongs to class } i, \\ 0, & \text{otherwise,} \end{cases}$$

and

$$f(\mathbf{x}) = \arg \min_i \chi_i(\mathbf{x}).$$

A major theoretical problem in machine learning is the so called curse of dimensionality - the complexity of the approximating model increases exponentially with the dimension of the input. Another theoretical problem is that if the class boundaries are not smooth or not well separated then the labeling function is not smooth, resulting again in an increased model complexity.

Manifold learning tries to ameliorate this problem by assuming that the data lies on some unknown, low dimensional manifold, on which the classes are well separated. With this assumption, there are well developed techniques to learn various quantities related to the manifold, in particular, the eigen-decomposition of the Laplace-Beltrami operator. Since these objects must be learnt from the data, these techniques are applicable in the semi-supervised setting, in which we have all the data points \mathbf{x}_j available in advance.

Recently, we have discovered [18] a more direct method to approximate functions on unknown manifolds without trying to learn anything about the manifold itself, and giving an approximation with theoretically guaranteed errors on the entire manifold; not just the points in the original data set. Our approximation has the form

$$\mathbf{x} \mapsto \sum_j (f(\mathbf{x}_j) + \epsilon_j) \tilde{\Phi}_{N,q}(|\mathbf{x} - \mathbf{x}_j|_{2,Q}) \quad (1.1)$$

where $\tilde{\Phi}_{N,q}$ is a specially constructed kernel, Q is the dimension of the ambient space, q is the dimension of the manifold, and $|\cdot|_{2,Q}$ is the Euclidean metric on \mathbb{R}^Q (see Section 3.1 for details). In the case when $N = 1$, our kernel reduces to the oft-used Gaussian kernel. In this paper, we prove how a more classical approach of empirical risk minimization or generalization error measured in the least squares sense using the kernel introduced in [18] leads to errors that show a gradual deterioration as one moves away from the training data, thereby yielding a heuristic to determine the parameter N .

In many applications, we can assume some further knowledge of the data distribution; in particular, that the data is sampled from an unknown sub-manifold of a known manifold. It is then natural to conjecture that one might be able to replace the Euclidean distance in (1.1) by the geodesic distance on the known manifold. While the theory analogous to the one in [18] seems difficult at this point, we formulate our main theorems in a greater abstraction to allow the study of pointwise errors using least squares approximation based on the resulting kernels. We demonstrate experimentally the effect of such a construction by considering each element of the FMCW radar data as a time series, which in turn may be identified with a point on a Grassman manifold using the ideas in [31].

Although our main focus is on the detection of hand gestures based on FMCW radar data, we include an additional example about classification in a simple video data in order to demonstrate the fact that our method is agnostic to the domain knowledge feature extraction.

To summarize, the main contributions of this paper are as follows:

- We examine pointwise errors in function approximation using empirical risk minimization and generalization error measured with least squared loss with a generalized version of the kernel introduced in [18].
- We demonstrate the performance of our theory in the very simple case of $N = 1$ (i.e., Gaussian kernel) in the case of hand gesture recognition based on FMCW radar data. Our results compare favorably with other known techniques, and give a fairly good accuracy in comparison with deep CNNs but at a substantially lower time complexity. Additionally, this provides new benchmark results on the recently published Dop-Net data set [25].
- Our method is agnostic to the domain knowledge, a fact which we demonstrate using classification in a simple video data.

In Section 2, we summarize the connection between our work and other related works, although not exhaustively. The technical background that motivates our work in this paper is explained in Section 3. In Section 4, we state our main theoretical results. The experimental results are presented in Section 5. The proofs of the results in Section 4 are given in Section 6.

2 Related works

We consider time-frequency images produced by the radar data or the frames of a video data as a time series. In former case, the x -axis is treated as time and the vertical cross section at each time then yields a time series. In [31], Turaga et. al. have proposed that such data may be considered as points on a Grassman manifold. This gives rise to the choice of various distances in our kernel.

We apply our kernel to micro-Doppler radar for gesture classification, which has seen a surge of interest due to the emergence of inexpensive Frequency Modulated Continuous Wave (FMCW) radars, which are now widely available. Micro-Doppler radar has found success in various applications related to classifying humans, animals and objects, such as activity monitoring, autonomous driving, and unmanned aerial vehicle detection [25, 35, 36, 29, 21]. The approach taken by practitioners is to use a time-frequency transform, such as the Short-Time Fourier Transform (STFT), to form an image and extract features or use directly with a neural network. In this paper, we assume that the time-frequency images can be explicitly mapped to points on an unknown manifold with a well defined metric, serving as a new feature representation. This is unlike current approaches which extract hand-crafted features to form vectors in Euclidean space or deep neural networks that automatically extract features with limited interoperability.

Hand crafted features are usually inspired by physics and taken to be measurements of frequency and/or time, such as the bandwidth of the micro-Doppler signature, its time duration, energy content, or various ratios and linear combinations of these or similar measurements [4, 29]. Alternatively, descriptive statistics such as the mean, variance, and higher order statistics are also commonly used [14]. There have also been efforts into defining new features through mathematical transforms, such as the discrete cosine transform, mel-frequencies, and other parameterized variations of these transforms [15]. The success of these approaches are by large determined by the application, radar system parameters, and quantity of training data. In [10], Gurbuz et al. study the effect of various micro-Doppler features, such as transmit frequency, range and Doppler resolution, antenna-target geometry, signal-to-noise ratio and dwell-time. While classifier performance on hand-crafted features undoubtedly depend on these parameters, the performance of more advanced feature extraction methods will also be affected by the size of the training set and distributional variation between the train and test data. For example, statistical variation within a class can depend on different measurement environments and subjects, which was not addressed in that study.

Thus, it is desirable to develop methods for feature extraction that are invariant to these types of within class variation. In our approach, we develop features using the left singular vectors of the spectrogram, representative of the discretized spectrogram’s column space. These features capture the frequency content of the micro-Doppler signature while imposing invariance with respect to the underlying time-series, which can better represent the discriminant attributes common to the entire data set. For example, we expect multiple samples corresponding to the same gesture can be represented by a collection of orthonormal basis matrices that are close under a particular metric. Furthermore, the subspace corresponding to a data sample can be viewed as subspace of a larger subspace spanned by the all the samples of the class.

Recently, deep learning architectures, such as CNNs have also been used for micro-Doppler applications [5, 12, 1, 37]. By design, CNNs are invariant to shifts in the two-dimensional image, obtained by using a combination of additive group convolutions and pooling operations. While relatively simple CNNs consisting of only three to five convolutional layers have been shown to be successful, deeper and more complex network approaches have also been investigated [26]. Furthermore, more advanced deep learning approaches have also been taken to compensate for limited training data, such as generating data using generative adversarial networks and transfer learning [22, 30].

We compare our approach to both hand-crafted features and CNNs, demonstrating that our approach outperforms physics based hand-crafted features, while under-performing a CNN, but at a significantly reduced computational cost during training. While we observe that the specific model we used outperforms on this data set and generalizes well, this is not necessarily the case for larger networks or different data sets. For example, in [30], the authors find that the SVM of the spectrogram outperforms much deeper networks like VGG-16. Additionally, unlike CNNs, features defined on a specific manifold through the kernel function provide a clear advantage in being able to more precisely obtain invariance to well defined nuisance transformations known a priori, based on knowledge of the application and data. This is complemented by theory that gives insight into generalization performance.

We will show in Section 4 that the process of empirical risk minimization with our kernel yields an exact reproduction of the label function for the training data. In this sense, the work is related to several recent works which have observed that it is possible to achieve a zero training error while keeping the test error under control. In the case of classification problems, Belkin, Hsu, and Mitra [3] analyze the “excess error” in least square fits by piecewise linear interpolants over that obtained by the optimal Bayes’ classifier. In [23, 24], the question is analyzed from the perspective of the geometry of the error surface with respect to different loss functions near the

local extrema. In particular, it is shown in [23] that substituting the ReLU activation function by a polynomial approximation exhibits the same behavior as the original network. In [20] we have analyzed the question from the point of view of approximation theory so as to examine the intrinsic features of the data (rather than focusing on specific training algorithms) that allow this phenomenon. A crucial role in the proofs of the results in that paper is played by a highly localized kernel. In this paper, we focus on the properties of a localized kernel in a much greater setting of a locally compact metric measure space that allow the results analogous to those in [20].

3 Technical background

In this section, we discuss some further technical details to motivate our main results in Section 4. In Section 3.1, we describe our constructions for approximation on an unknown sub-manifold of the Euclidean space. In Section 3.2, we provide a mathematical model for the Doppler radar measurements, leading to the need for examining our results in Section 3.1 to the case of a sub-manifold of a known manifold, namely, the Grassman manifold. In Section 3.3, we describe the ideas in [31] that leads to the Grassman manifold again from a different perspective of time series classification.

3.1 Approximation on manifolds

In this section, we describe our construction for a direct method for function approximation on a sub-manifold of a Euclidean space, without resorting to a two step procedure involving the estimation of quantities related to the manifold such as coordinate charts or eigen-decomposition of the Laplace-Beltrami operator. Our construction involves a localized kernel based on Hermite polynomials.

These are defined by the Rodrigues' formula (cf. [28, Eqns. (5.5.3), (5.5.1)])

$$h_k(x) = \frac{(-1)^k}{\pi^{1/4} 2^{k/2} \sqrt{k!}} \exp(x^2) \frac{d^k}{dx^k} \exp(-x^2).$$

However for relatively small values of k and $|x| < \sqrt{2k}$, they are most efficiently computed using the recurrence relations:

$$\begin{aligned} h_k(x) &:= \sqrt{\frac{2}{k}} x h_{k-1}(x) - \sqrt{\frac{k-1}{k}} h_{k-2}(x), \quad k = 2, 3, \dots, \\ h_0(x) &:= \pi^{-1/4}, \quad h_1(x) := \sqrt{2} \pi^{-1/4} x. \end{aligned} \quad (3.1)$$

We write

$$\psi_k(x) := h_k(x) \exp(-x^2/2), \quad x \in \mathbb{R}, \quad k \in \mathbb{Z}_+. \quad (3.2)$$

The functions $\{\psi_k\}_{k=0}^\infty$ are an orthonormal set with respect to the Lebesgue measure. In the sequel, we fix an infinitely differentiable function $H : [0, \infty) \rightarrow [0, 1]$, such that $H(t) = 1$ if $0 \leq t \leq 1/2$, and $H(t) = 0$ if $t \geq 1$. Further, let $Q \geq q \geq 1$ be fixed integers. We define for $x \in \mathbb{R}$, $m \in \mathbb{Z}_+$:

$$\mathcal{P}_{m,q}(x) := \begin{cases} \pi^{-1/4} (-1)^m \frac{\sqrt{(2m)!}}{2^m m!} \psi_{2m}(x), & \text{if } q = 1, \\ \frac{1}{\pi^{(2q-1)/4} \Gamma((q-1)/2)} \sum_{\ell=0}^m (-1)^\ell \frac{\Gamma((q-1)/2 + m - \ell)}{(m-\ell)!} \frac{\sqrt{(2\ell)!}}{2^\ell \ell!} \psi_{2\ell}(x), & \text{if } q \geq 2, \end{cases} \quad (3.3)$$

and the kernel $\tilde{\Phi}_{N,q}$ for $x \in \mathbb{R}$, $N > 0$ by

$$\begin{aligned} \tilde{\Phi}_{N,q}(x) &:= \sum_{m=0}^{\lfloor N^2/2 \rfloor} H\left(\frac{\sqrt{2m}}{n}\right) \mathcal{P}_{m,q}(x) \\ &= \frac{1}{\pi^{(2q-1)/4} \Gamma((q-1)/2)} \sum_{\ell=0}^N \left\{ \sum_{j=0}^{N-\ell} H\left(\frac{\sqrt{2(m+j)}}{n}\right) \frac{\Gamma((q-1)/2 + j)}{j!} \right\} \psi_{2\ell}(0) \psi_{2\ell}(x) \end{aligned} \quad (3.4)$$

The kernel $\tilde{\Phi}_{N,q}(x)$ can be computed easily and efficiently using the second equation in (3.4), and the Clenshaw algorithm [9, p. 79].

Constant convention

In the sequel, the notation $A \lesssim B$ (equivalently, $B \gtrsim A$) will mean that $A \leq cB$ for some positive constant c depending only on fixed objects under discussion such as q , Q , the parameter S to be introduced later, and the manifold/spaces/measures/distances to be described later. The notation $A \sim B$ means $A \lesssim B$ and $B \lesssim A$.

Next, let \mathbb{X} be a q dimensional, compact, connected, orientable, sub-manifold of \mathbb{R}^Q , ρ be the geodesic distance on \mathbb{X} , μ^* be its volume element. We will abbreviate our notation and write $\Phi_N^M(\mathbf{x}) = \Phi_{N,q}^M(|\mathbf{x}|_{2,Q})$, $\mathbf{x} \in \mathbb{X}$ ¹.

Let $C(\mathbb{X})$ denote the class of all continuous real valued functions on \mathbb{X} equipped with the supremum norm $\|f\|_\infty := \max_{x \in \mathbb{X}} |f(x)|$. Using the kernel Φ_N^M , we define an integral operator, analogous to a convolution operator on $C(\mathbb{X})$ by

$$\sigma_N^M(f)(\mathbf{x}) := \int_{\mathbb{X}} \Phi_N^M(\mathbf{x} - \mathbf{y}) f(\mathbf{y}) d\mu^*(\mathbf{y}), \quad N > 0. \quad (3.5)$$

(In the notation of [18], $\sigma_N^M(f) = \sigma_{N,1}(\mathbb{X}; f)$.) We are interested in approximation of Lipschitz continuous functions on \mathbb{X} ; i.e., functions $f \in C(\mathbb{X})$ for which for which

$$\|f\|_{\text{Lip}} := \sup_{\substack{\mathbf{x}, \mathbf{x}' \in \mathbb{X} \\ \mathbf{x} \neq \mathbf{x}'}} \frac{|f(\mathbf{x}) - f(\mathbf{x}')|}{\rho(\mathbf{x}, \mathbf{x}')} < \infty. \quad (3.6)$$

A consequence of [18, Theorem 8.1] is the following.

Theorem 3.1 *Let $f \in \text{Lip}(\mathbb{X})$. For $N \geq 1$, we have*

$$\|f - \sigma_N^M(f)\|_\infty \lesssim \frac{\|f\|_{\text{Lip}}}{N}. \quad (3.7)$$

An important ingredient in the proof of Theorem 3.1 is the following proposition proved in [18, Corollary 6.1], and reformulated using the fact that $|\mathbf{x} - \mathbf{y}|_{2,Q} \sim \rho(\mathbf{x}, \mathbf{y})$ for $\mathbf{x}, \mathbf{y} \in \mathbb{X}$ [18, Corollary 8.1].

Proposition 3.1 *Let $S > q$. The kernel Φ_N^M defined in (3.4) satisfies each of the following properties.*

$$|\Phi_N^M(\mathbf{x} - \mathbf{y})| \lesssim \frac{N^q}{\max(1, (N\rho(\mathbf{x}, \mathbf{y}))^S)}, \quad \mathbf{x} \in \mathbb{R}^q, \quad (3.8)$$

$$|\Phi_N^M(\mathbf{0})| \sim N^q, \quad |\Phi_N^M(\mathbf{x})| \lesssim N^q, \quad |\Phi_N^M(\mathbf{x}) - \Phi_N^M(\mathbf{y})| \lesssim N^{q+1} \|\mathbf{x}\|_{2,Q} - \|\mathbf{y}\|_{2,Q}, \quad \mathbf{x}, \mathbf{y} \in \mathbb{R}^Q. \quad (3.9)$$

Motivation 1: *In practice, of course, one needs to use a discretization of the integral in (3.5). Obviously, an accurate discretization would require the knowledge of the values of f at a sufficiently large number of points in \mathbb{X} . In Doppler radar applications, one has only a small amount of data, so that the above theorem cannot be used effectively in a direct manner.*

3.2 Micro-Doppler radar signals

In this section we denote the radar location by $\mathbf{x} \in \mathbb{R}^3$ and the target location by $\mathbf{y} \in \mathbb{R}^3$. We assume that at $t = 0$ the object is initially located at $\mathbf{y}_0 \in \mathbb{R}^3$. During the collection period $t \in [0, T]$, the target undergoes motion defined by a displacement with velocity $\mathbf{v} \in \mathbb{R}^3$ and a rotation given by the matrix $\mathbf{R}(t)$. Thus, at time t the location of the object is

$$\mathbf{y}(t) = \mathbf{R}(t)\mathbf{y}_0 + \mathbf{v}t. \quad (3.10)$$

Assuming the radar transmits in free space, the received signal is the convolution of the scalar wave equation Green's function with the transmitted signal $p(t)$, given by

$$s(t) = \int p(t - \|\mathbf{x} - \mathbf{y}(t)\|_2) \rho(\mathbf{y}(t)) d\mathbf{y}(t), \quad (3.11)$$

¹We note that when $N = 1$, $\Phi_N^M(\mathbf{x})$ reduces to just a constant multiple of $\exp(-|\mathbf{x}|^2/2)$.

where $p(t)$ is the transmitted waveform and $\rho(\mathbf{y})$ is the reflectivity function, modeling the scattering behavior of the target.

Assuming there are only a finite number of isotropic scattering locations², we model the reflectivity function as

$$\rho(\mathbf{y}) = \sum_{k=1}^K K \delta(\mathbf{y}(t) - \mathbf{y}_k(t)) \rho_k, \quad (3.12)$$

where $y_k(t)$ is the k -th scatterer at time t and $\rho_k \in \mathbb{R}^+$ is the amplitude of the scatterer, and K is the number of scattering locations. Using (3.10) and (3.12) in (3.11), we obtain

$$s(t) = \sum_{k=1}^K K p(t - \|\mathbf{x} - \mathbf{R}_k(t) \mathbf{y}_{0,k} - \mathbf{v}_k t\|_2) \rho_k + n(t). \quad (3.13)$$

where $n(t)$ represents noise, clutter, and small amplitude interfering signals when the isotropic point scattering assumption (3.12) does not precisely hold.

Typically, $p(t)$ is a continuous waveform (CW), possibly with frequency modulation (FMCW), defined as

$$p(t) = e^{i(\omega_c t + \frac{1}{2} \alpha t^2)}, \quad (3.14)$$

where ω_c is the carrier frequency and α is the chirp rate. The data set introduced in [25] and used in our experiments, were collected with a FMCW waveform.

In (3.13), each $\mathbf{y}_{0,k}$ represents the initial scattering locations of the object that contribute to the signal measured at the receiver. For gesture recognition K will be small since there are only a small number of dominant scattering locations. Thus, the received signal $s(t)$ will lie in a low-dimensional subspace given by the span of the individual received signals for each scatterer, of maximum dimension K . This is due to the fact that the scattered signals are approximately orthogonal for large ω_c used for micro-Doppler radars, and motivates our following choice of features.

Generally, micro-Doppler signal classification is accomplished using the spectrogram of (3.13), defined as

$$D(\omega, \tau) = \int_{\mathbb{R}} s(t + \tau) w(t) e^{-i\omega(t+\tau)} dt, \quad (3.15)$$

where w is a smooth window function. In practice, (3.13) will be sampled to form a discrete time-series, and one uses the discrete version of (3.15):

$$\mathbf{D} = \mathbf{F} \mathbf{W} \mathbf{S}, \quad (3.16)$$

where \mathbf{F} is a partial Fourier matrix, $\mathbf{W} = \text{diag}(\mathbf{w})$ is a diagonal matrix consisting of the elements of \mathbf{w} , and $\mathbf{S} = [\mathbf{s}_1, \mathbf{s}_2, \dots, \mathbf{s}_N]$. The columns of \mathbf{D} correspond to the discrete Doppler frequencies $\omega_{-M/2}, \dots, \omega_{M/2}$, and the rows correspond to the discrete time points τ_0, \dots, τ_N .

Let the singular value decomposition of \mathbf{D} be given by

$$\mathbf{D} = \mathbf{U} \mathbf{\Sigma} \mathbf{V}, \quad (3.17)$$

where \mathbf{U} , \mathbf{V} are unitary matrices, and $\mathbf{\Sigma}$ is a diagonal matrix consisting of the singular values. In view of the results described in more detail in [32], we may consider the first r columns of \mathbf{U} to be a feature vector \mathbf{U}_r for the signal D in (3.15). We note that this feature vector is a point on the Grassman manifold $\mathcal{G}(r, N)$.

3.3 Representation of a general time series

The autoregressive-moving-average (ARMA) is a well-known dynamic model for time series data that parametrises a signal $f(t)$ by the equations

$$f(t) = C z(t) + w(t), \quad w(t) \sim \mathcal{N}(0, R) \quad (3.18)$$

$$z(t+1) = A z(t) + v(t), \quad v(t) \sim \mathcal{N}(0, Q) \quad (3.19)$$

where $z \in \mathbb{R}^d$ is the hidden state vector, $f : \mathbb{R} \rightarrow \mathbb{R}^p$, $d \leq p$ is the hidden state dimension, and $N(0, \sigma)$ denotes a normal distribution with mean zero and standard deviation σ [31]. There are widely-used closed form solutions for estimating the parameters A and C in terms of the singular value decomposition $[f(1), \dots, f(\tau)] = U \Sigma V^T$, namely,

$$C = U, \quad A = \Sigma V^T D_1 V (V^T D_2 V)^{-1} \Sigma^{-1}, \quad (3.20)$$

²Isotropic scattering means the signal is reflected in all directions, a reasonable assumption for small scattering locations on the human hand.

where

$$D_1 = \begin{pmatrix} 0 & 0 \\ I_{\tau-1} & 0 \end{pmatrix}, \quad D_2 = \begin{pmatrix} I_{\tau-1} & 0 \\ 0 & 0 \end{pmatrix}.$$

It can be shown [31] that the expected observation sequence is given by

$$O_\infty = \mathbb{E} \left[\begin{pmatrix} f(0) \\ f(1) \\ f(2) \\ \vdots \end{pmatrix} \right] = \begin{bmatrix} C \\ CA \\ CA^2 \\ \vdots \end{bmatrix} z(0) \quad (3.21)$$

Thus, by truncating the matrix O_∞ up to m -th block for some m , one can represent the time series f as point on the Grassman manifold $\mathcal{G}(d, mp)$.

Motivation 2: Clearly, the set of time series of interest, such as the low rank representations of the micro-Doppler radar signals, is only an unknown subset of the Grassman manifold, rather than the entire manifold. Assuming that this subset is a sub-manifold, it is interesting to examine the span of $\{\tilde{\Phi}_{N,q}(\rho(\circ, \mathbf{y}_j))\}_{j=1}^M$, where ρ is the geodesic distance on the Grassman manifold.

4 Theoretical results

Our goal in this section is to formulate results for approximation based on a small amount of data. We will examine two tools for this purpose: empirical risk minimization, and theoretical least square loss. In each case, we will obtain pointwise error estimates which indicate how the error deteriorates as the input variable moves away from the training data. Our estimates will give a deeper insight into which features of the data give rise to what accuracy *intrinsically*, as opposed to many results in the literature that depend upon the method used to solve the optimization problems involved. In view of the motivation given in Section 3.3, we will state our results in greater abstraction than in the context of the motivation given in Section 3.1.

Let \mathbb{X} be a locally compact metric measure space, with metric ρ , and a distinguished measure μ^* . As before, $C(\mathbb{X})$ denotes the space of bounded and uniformly continuous real valued functions on \mathbb{X} , equipped with the supremum norm: $\|f\|_\infty = \sup_{x \in \mathbb{X}} |f(x)|$. The class $\text{Lip}(\mathbb{X})$ of Lipschitz functions comprises $f \in C(\mathbb{X})$ for which

$$\|f\|_{\text{Lip}} := \sup_{\substack{\mathbf{x}, \mathbf{x}' \in \mathbb{X} \\ \mathbf{x} \neq \mathbf{x}'}} \frac{|f(\mathbf{x}) - f(\mathbf{x}')|}{\rho(\mathbf{x}, \mathbf{x}')} < \infty. \quad (4.1)$$

Definition 4.1 Let $S > q \geq 1$ be integers. A family of kernels $\{\Phi_N : \mathbb{X} \times \mathbb{X} \rightarrow \mathbb{R}\}$ is called (q, S) -**localized** if each Φ_N is symmetric, and

$$|\Phi_N(x, y)| \lesssim \frac{N^q}{\max(1, (N\rho(x, y))^S)}, \quad (4.2)$$

where the constant involved in \lesssim may depend upon q and S but not on N , x , or y . With an abuse of terminology we will say that Φ_N is (q, S) -localized.

Remark 4.1 Kernels satisfying (4.2) are known in many contexts. The kernel denoted by Φ_N^M in Section 3.1 is one example. Many other constructions in different contexts are discussed in [19] and references therein. ■

Remark 4.2 In the remainder of this paper, we will treat q and S to be fixed and all the constants may depend upon these. In particular, we will omit the qualification (q, S) and refer to Φ_N as a localized kernel. ■

Let $M \geq 1$ be an integer, $\mathcal{C} = \{y_1, \dots, y_M\} \subset \mathbb{X}$. We are interested in studying approximation of Lipschitz functions on \mathbb{X} from the space

$$\mathcal{V}(\mathcal{C}) = \text{span}\{\Phi_N(\circ, y_j)\}_{j=1}^M. \quad (4.3)$$

Remark 4.3 If $\Phi_N(x, y)$ admits a Mercer expansion of the form $\sum \lambda_k \phi_k(x) \phi_k(y)$, and the set \mathcal{C} is sufficiently dense in \mathbb{X} , then in a number of cases as in [19], the space $\mathcal{V}(\mathcal{C})$ is the same as $\text{span}\{\phi_k : \lambda_k \lesssim N\}$. However, our interest in this paper is when \mathcal{C} has a large minimal separation rather than being dense. ■

We will study the behavior of approximations defined by the solutions of two minimization problems:

The **empirical risk** minimizer is defined to be

$$P_E(\mathcal{V}(\mathcal{C}); f) := \arg \min_{P \in \mathcal{V}(\mathcal{C})} \sum_{k=1}^M |f(y_j) - P(y_j)|^2. \quad (4.4)$$

If τ is a probability measure on \mathbb{X} , **theoretical least square loss** minimizer is defined by

$$P_T(\tau, \mathcal{V}(\mathcal{C}); f) := \arg \min_{P \in \mathcal{V}(\mathcal{C})} \int_{\mathbb{X}} |f(y) - P(y)|^2 d\tau(y). \quad (4.5)$$

We need to assume some further conditions on the kernels $\{\Phi_N\}$.

Definition 4.2 Let $S > q \geq 1$ be integers. A family of kernels $\{\Phi_N\}$ is called **admissible** if it is (q, S) -localized and satisfies each of the following properties.

$$|\Phi_N(y, y)| \sim N^q, \quad y \in \mathbb{X}. \quad (4.6)$$

$$\begin{aligned} |\Phi_N(x, y) - \Phi_N(x', y)| &\lesssim N^{q+1} \rho(x, x'), & x, x', y \in \mathbb{X}, \\ |\Phi_N(x, y) - \Phi_N(x, y')| &\lesssim N^{q+1} \rho(y, y'), & x, y, y' \in \mathbb{X}. \end{aligned} \quad (4.7)$$

With an abuse of terminology as before, we refer to any member Φ_N of an admissible family as an admissible kernel.

Remark 4.4 The kernel denoted by Φ_N^M in Section 3.1 is one example of admissible kernels (cf. Proposition 3.1). Several other examples are available in the literature, for example, based on eigenfunctions of the Laplace-Beltrami operator on manifolds ([7, 8]). ■

In the study of approximation properties of both the empirical risk minimizer and theoretical least squares loss minimizer, a crucial role is played by the minimal separation among the points in \mathcal{C} , defined by the minimal separation among the points defined by

$$\eta(\mathcal{C}) = \min_{1 \leq j \neq k \leq M} \rho(\mathbf{y}_j, \mathbf{y}_k), \quad (4.8)$$

In order to state our main theorems, we need to make some further assumptions.

For $x \in \mathbb{X}$, $r > 0$, we write

$$\mathbb{B}(x, r) = \{y \in \mathbb{X} : \rho(x, y) \leq r\}, \quad \Delta(x, r) = \mathbb{X} \setminus \mathbb{B}(x, r). \quad (4.9)$$

We assume that there exists $q \geq 0$ such that

$$\mu^*(\mathbb{B}(x, r)) = \mu^*(\{y \in \mathbb{X} : \rho(x, y) < r\}) \lesssim r^q, \quad x \in \mathbb{X}, r > 0, \quad (4.10)$$

and

$$\mu^*(\mathbb{B}(x, r)) \gtrsim r^q, \quad x \in \mathbb{X}, 0 < r \leq 1. \quad (4.11)$$

It is shown in [19] that in the case when \mathbb{X} is a manifold as described earlier, the condition (4.11) is satisfied in fact for all $r \leq \text{diam}(\mathbb{X})$. The condition (4.10) is satisfied in many cases when \mathbb{X} is a smooth compact connected q -dimensional manifold, ρ is the Riemannian metric, and μ^* denotes the volume measure.

Our first theorem derives pointwise error estimates for the empirical risk minimizer..

Theorem 4.1 Let $\{\Phi_N\}$ be a family of admissible kernels, and (4.10) and (4.11) be satisfied. Let $x \in \mathbb{X}$, $\delta(x) = \min_{1 \leq j \leq M} \rho(x, y_j)$, and $\tilde{\eta} = \min(1, \eta(\mathcal{C}))$. Let $F \in \text{Lip}(\mathbb{X})$. There exists a constant $C > 0$ independent of F , N , and \mathcal{C} such that if $N \geq C\eta(\mathcal{C})^{-1}$, then there exists a unique empirical risk minimizer $P_E(\mathcal{V}(\mathcal{C}); F)$ that satisfies

$$P_E(\mathcal{V}(\mathcal{C}); F)(y_j) = F(y_j), \quad j = 1, \dots, M. \quad (4.12)$$

We have the following error estimates.

If $\delta(x) > \tilde{\eta}/3$ then

$$|P_E(\mathcal{V}(\mathcal{C}); F)(x)| \lesssim \frac{\|F\|_\infty}{(N\tilde{\eta})^S}. \quad (4.13)$$

If $\delta(x) \leq \tilde{\eta}/3$ then

$$|P_E(\mathcal{V}(\mathcal{C}); F)(x) - F(x)| \lesssim (N + \|f\|_{\text{Lip}}) \delta(x) + \|F\|_\infty (N\tilde{\eta})^{q-S}. \quad (4.14)$$

Here, the constants involved are independent of F and x .

To describe the analogue of Theorem 4.1 for the minimizer of the theoretical least square loss, we need some further notation relevant to the normal equations for the minimization problem. We define

$$\Psi_N(x, y) = \int_{\mathbb{X}} \Phi_N(x, z) \Phi_N(y, z) d\tau(z), \quad N > 0, \quad x, y \in \mathbb{X}, \quad (4.15)$$

and for $f \in C(\mathbb{X})$,

$$\sigma_N(f)(x) = \int_{\mathbb{X}} f(y) \Phi_N(x, y) d\mu^*(z). \quad (4.16)$$

We note that if τ is absolutely continuous with respect to μ^* with the Radon-Nikodym derivative f_0 , then the normal equations for the theoretical least squares loss minimization are

$$\sum_{\ell=1}^M a_\ell \Psi_N(y_\ell, y_j) = \sigma_N(f f_0)(y_j), \quad j = 1, \dots, M. \quad (4.17)$$

Theorem 4.2 *We assume the set up as in Theorem 4.1. Let τ be absolutely continuous with respect to μ^* with $d\tau = f_0 d\mu^*$ for some $f_0 \in C(\mathbb{X})$, $f_0(z) \geq m(f_0) > 0$ for all $z \in \mathbb{X}$. There exists a constant $C > 0$ independent of F , N , and \mathcal{C} such that if $N \geq C\eta(\mathcal{C})^{-1}$, then there exists a unique theoretical least square loss risk minimizer $P_T(\tau, \mathcal{V}(\mathcal{C}); F)$ that satisfies the following error estimates.*

If $\delta(x) > \tilde{\eta}/3$ then

$$|P_E(\mathcal{V}(\mathcal{C}); F)(x)| \lesssim \frac{\|f_0 F\|_\infty}{(N\tilde{\eta})^S}. \quad (4.18)$$

If $\delta(x) = \rho(x, y_\ell) \leq \tilde{\eta}/3$ then

$$\begin{aligned} & \left| P_T(\tau, \mathcal{V}(\mathcal{C}); F)(x) - \frac{\Phi_N(x, x)}{\Psi_N(y_\ell, y_\ell)} f_0(x) F(x) \right| \\ & \lesssim (N\eta)^{q-S} \|f_0 F\|_\infty + \|f_0 F - \sigma_N(f_0 F)\|_\infty + (N + \|f_0 F\|_{Lip}) \delta(x). \end{aligned} \quad (4.19)$$

Here, the constants involved are independent of F and x .

Remark 4.5 In the case of the kernels Φ_N^M , the quantity $\|f_0 F - \sigma_N(f_0 F)\|_\infty$ is estimated by Theorem 3.1. Similar estimates exist also in the other examples described in [19] with other conditions on f_0 and F . ■

Remark 4.6 We note that (4.13) and (4.18) show that one does not expect a good approximation to F as $N \rightarrow \infty$ in the region away from the points \mathcal{C} . On the other hand, (4.14) and (4.19) show that the approximation actually deteriorates if $N \rightarrow \infty$. The balance of the various terms on the right hand side of these estimates gives us some insight into the choice of N as well as how the approximation error deteriorates as x is further and further away from \mathcal{C} . This phenomenon is caused by the localization of the kernels, resulting in overfitting the data if N is very large. In our experiments in Section 5, we will need to use $N = 1$; the higher values of N led to overfitting. ■

5 Experimental Results

In this section, we describe the use of the minimization problems discussed in Section 4 in the context of gesture recognition with micro-Doppler radar readings (Section 5.1), and to demonstrate the fact the theory is applicably agnostic to the domain knowledge, also in the context of a small video data set (Section 5.2). As remarked before, we use the kernel $\tilde{\Phi}_{N,q}(\rho(x, y)^2)$ with different distances $\rho(x, y)$, but only with $N = 1$, since higher values led to overfitting.

5.1 Gesture recognition

We describe the data set in Section 5.1.1. The data involves 4 gestures made by 6 persons. We focus first on recognition of gestures independently of the person making the gesture. The pre-processing step is described in Section 5.1.2. The methodology of the experiments as well as the results are described in Section 5.1.3. The effect of choosing the dimension of the manifold is discussed in Section 5.1.4. The effect of choosing various percentage of the training data is described in Section 5.1.5. In Section 5.1.6, we examine the results of training on all the gestures made by 5 of the subjects, and predicting the results for the corresponding gesture by the 6th subject.

5.1.1 Data set

We use the publicly available micro-Doppler data set *Dop-NET* distributed by University College London Radar group [25]. The data set consists of complex spectrograms formed using the motion compensated, measured micro-Doppler signatures of five people performing four different hand gestures: snap, wave, pinch, click. The data is obtained using a linear FMCW waveform at 24 GHz center and 750 MHz bandwidth. While a training and test set are provided, no ground truth values are given, therefore, in all our trials we randomly split the data into train and test groups.

In Figure 1, an example spectrogram is shown for each class. Since the time duration of each gesture varies the number of columns in each sample can vary by up to an order of magnitude. Furthermore, we note that there are visible similarities between the classes; for example, the pinch and click gesture are both short duration with most of the energy concentrated over a small region in time, while the swipe and wave gestures last for longer duration and show more oscillatory behavior in the case of wave. Clearly, these similarities make this classification problem particularly difficult, and motivate the use of features that are robust to the varying time duration and small variation in the Doppler frequencies.

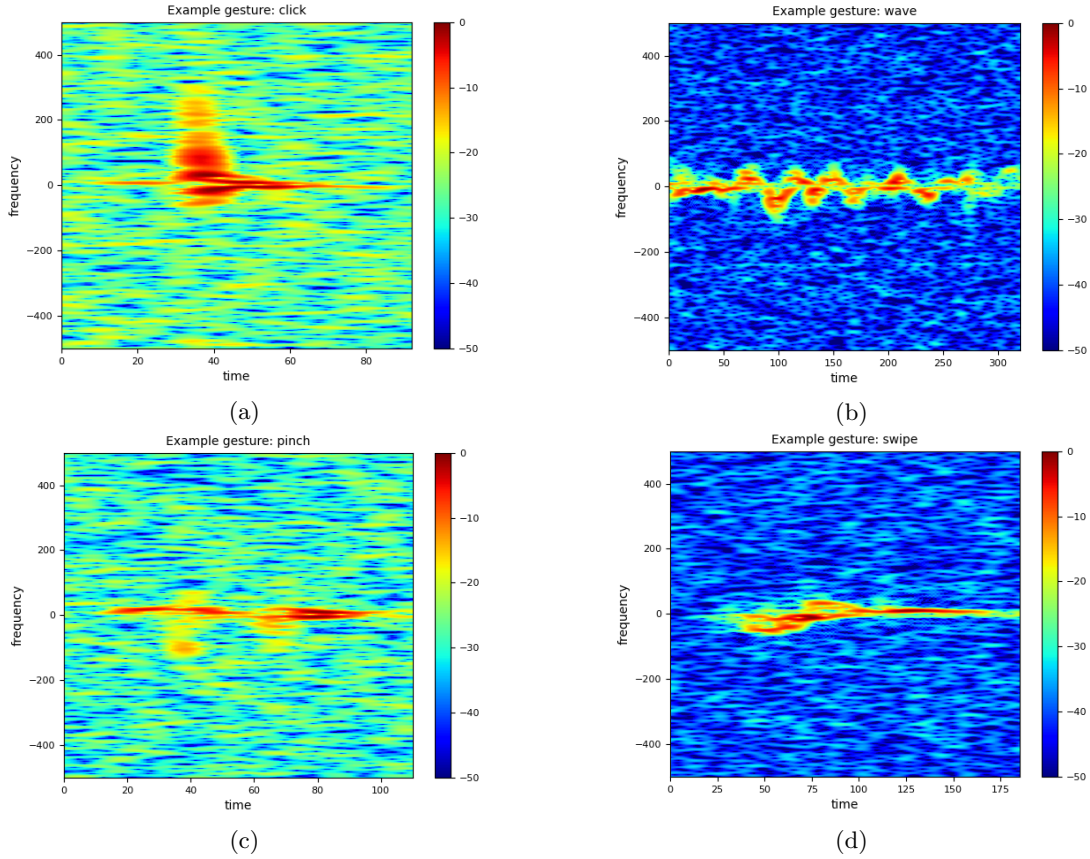


Figure 1: Examples of one realization for each class. a) Click. b) Wave. c) Pinch. d) Swipe.

5.1.2 Data Preprocessing

Prior to classification, we perform data preprocessing to reduce noise and clutter, and further normalize to account for variation in the dynamic range. To reduce noise and clutter we used Yen’s method which is a global binary threshold algorithm used in image processing [33], finding that it performed best over other image processing techniques, as well the envelope detection approach proposed in [34]. For the k th data sample X_k , the output of this process is

$$\tilde{X}_k = \mathcal{T} \{20 \log_{10} (|X_k|)\} \quad (5.1)$$

where \mathcal{T} denotes the thresholding operator implemented as in [33].

Next, we normalize the data to account for variation in the dynamic range. Starting with (5.1) we considered two approaches: normalizing the data into the range $[0, 1]$ and forming a binary representation. Unlike the normalized

data, the binary representation provides information only on the support of the signal in the time-frequency plane, but provides the advantage of reduced memory requirements for storage.

In addition to this normalization, we also compared the performance of the kernels with hand-crafted features instead. For the case of handcrafted features, we define a feature vector in \mathbb{R}^3 , consisting of [34]:

$$B = f_h - f_l, \quad T = T_2 - T_1, \quad R = \frac{f_h}{f_l}, \quad (5.2)$$

where f_l, f_h, T_1, T_2 are the minimum frequency, maximum frequency, start and end time of the micro-Doppler signature, chosen to capture 90% of the energy in frequency and time, respectively.

5.1.3 Performance Accuracy and Time Complexity

In our experiments, we test the Laplace SVD kernel, Gaussian SVD kernel and the Grassman kernel summarized in Table 1 using both the normalized and binary data. The details are as follows. Let X_1, X_2 be two matrices, and $X_i = U_i \Sigma_i V_i^T$, $i = 1, 2$ be the corresponding singular value decompositions. The kernels used in this paper are presented in Table 1, where r is the number of singular values used; i.e., the number of columns of U_i , and $\|\cdot\|_F$ denotes the Frobenius norm. We compared these approaches with a representative exemplar of the two common

Kernel Type	Expression	Parameters
Grassmann kernel	$\exp(-\gamma(r - \ U_1^T U_2\ _F^2))$	$\gamma = 0.2$
Laplace kernel	$\exp(-\alpha\ U_1 - U_2\ _F - \beta\ \Sigma_1 - \Sigma_2\ _F)$	$\alpha = 0.2, \beta = 0.0042$
Gaussian kernel	$\exp(-\alpha\ U_1 - U_2\ _F^2 - \beta\ \Sigma_1 - \Sigma_2\ _F^2)$	$\alpha = 0.2, \beta = 0.12$

Table 1: The definition of various kernels.

approaches: hand crafted features and convolutional neural networks (CNNs).

The CNN is chosen to consist of three convolution layers with ReLU activation functions and 2×2 pooling. We only use it with the pre-processed spectrograms and not the hand-crafted features (5.2). The filters are $10 \times 20 \times 20$, $40 \times 10 \times 10$, and $80 \times 5 \times 5$, respectively. The output of the convolution layers goes through an average pooling to form 5×5 representations for each filter, which results in feature vectors embedded in a manifold in \mathbb{R}^{2000} , which was chosen to be close to 2423, the maximum dimension of the support vector machine. Predictions were made using a dense layer and soft-max function, trained with cross-Entropy minimization using the ADAM optimizer and implemented using PyTorch library. We experimented using networks with increased feature dimension, but this led to over-fitting due to the small size of the data set, making it unlikely that a deeper, more complex network would be able to perform better.

In our experiments, we use a support vector machine with each kernel listed in Table 1 and the hand-crafted features given in (5.2). The results are averaged over five trials and the mean and variance for the classification accuracy, training time, and inference time are recorded in Table 2. In each experiment, the training set consists of 80% the data and the test set is the remaining 20%. The results using either binary or normalized pre-processed data are given in Tables 2a and 2b, respectively. While the choice of preprocessing does not impact the performance of the algorithms beyond a range of 1 – 3% in terms of accuracy and computational time for training and testing, the variance of the accuracy only varied from 0 – 0.07%, suggesting preprocessing does have a meaningful effect on performance. This is most pronounced in the case of the Laplacian and Grassman kernel, specifically, the Laplacian kernel outperforms the Grassman kernel by 3% for the binary data, and the opposite for the normalized data.

Furthermore, we find that the handcrafted features perform worst at classification with accuracy of $\sim 57.0/56.34\%$ for the binary and normalized data respectively. The CNN performs the best obtaining $\sim 95.44/96.34$ accuracy, while the kernel methods performed competitively with accuracy of 84.23 – 91.58%. The Gaussian kernel performed the best in both cases, reaching 91.58% and the Grassman kernel scoring the lowest at 84.23 on the binary preprocessed data. We attribute this to the fact that the binary data reduces the representative power of the Grassman kernel by restricting the amount of variation in the column space of the images, a consequence of the fact that each pixel can only take values on the edges of the interval, unlike the normalized data. This further suggests that by restricting the Grassmannian to a sub-manifold leads to improved performance. This is expected as the data points can better represent the smaller space.

While the CNN outperforms in terms of classification, this should be considered in the context of the cost of increased parameterization and computational time. The convolutional layers consist of a total of approximately 10, 100, 000 parameters which much be stored, opposed to the number of support vectors which is at most the 2423.

Approach (Binary)	Average Accuracy (%)	Train Time (s)	Test Time (s)
Laplace SVM	88.71±0.02	199.31±261.53	56.65±0.1
Gaussian SVM	91.58±0.0	137.92±3.39	43.3±0.2
Grassman SVM	84.23±0.01	104.11±0.54	34.58±0.24
HC Features SVM	57.0±0.09	0.2±0.0	0.07±0.0
CNN	95.44±0.01	3229.95±128.1	12.57±1.04

(a)

Approach (Normalized)	Accuracy (%)	Train Time (s)	Test Time (s)
Laplace SVM	85.09±0.01	261.84±16.52	75.85±6.27
Gaussian SVM	89.49±0.01	148.8±1.05	45.5±0.08
Grassman SVM	87.47±0.07	104.98±0.46	35.67±0.07
HC Features SVM	56.43±0.03	0.2±0.0	0.07±0.0
CNN	96.34±0.03	3266.99±194.04	13.93±0.29

(b)

Figure 2: The performance accuracy, training time, and testing time as well as variance (written as accuracy±variance) for each of the methods considered and different pre-processing schemes. a) Results for binary data. b) Results for normalized data.

The training time of the CNN is also three orders of magnitude larger than the kernel approach, noting that these computational times are reported for the case when the CNN is trained on a GPU and tested on the CPU³. If the CNN was trained on the CPU the difference in computational time would be even more drastic.

Even though number of parameters in the network is large, the network operates directly on the preprocessed spectrograms and does not require a singular value decomposition (SVD) to extract features, which has been taken into account in our timing results by including the SVD operation to construct the kernels in the reported computational times. However, despite these differences, the CNN is only three times faster and takes only 12 – 13 seconds instead of 34 – 56 seconds to perform inference for the kernel methods. We consider this difference to be negligible, attributing it to the fact that the Sci-Kit Learn library used to implement the SVM is purely written in python, while the CNN implemented in Pytorch, which has back-end highly optimized in C++. Thus, we conclude that the kernel methods can be viewed as trading off accuracy at the expense of increased computational efficiency and interoperability.

5.1.4 Sensitivity to Feature Dimension

The dimension of the data manifold is given by q and equal to the total number of left singular vectors. In this section, we investigate how well dimension $r < q$ performs, which we do by retaining only r singular vectors for the features used in the kernels defined in Table 1. Ideally, r should be chosen large enough to retain a sufficient amount of information required for optimal classifier performance. To better understand why this is the case, observe that the left singular vectors are the eigenvectors of the sample covariance matrix of the time windowed Fourier transform of the signal. Due to the similarity with principal component analysis, we expect that the feature will represent the data well if r is chosen to capture most of the energy.

In Figure 3, we show the average value of singular values plotted for each gesture. Clearly, for each gesture and pre-processing technique there is a sharp drop before $r = 20$ and the rest of the singular values are near zero. This suggests that the dimension of the subspace features need not be large, as expected based on the micro-Doppler structure described in Section 3.2. Thus, we investigate the performance of the manifold learning approach for varying values of r .

In Figure 4 we plot the average classification error when setting $r = 1, \dots, 20$ for the different preprocessing technique used with SVD Gaussian, SVD Laplace and Grassmannian kernel. For $r = 1$ all the SVD kernels underperform the Grassman kernels by approximately 10%, but then start to reduce the discrepancy in accuracy for $r = 2$ to $r = 9$. In this range the Gaussian kernel is minimal at $r = 3$ and $r = 4$ for the the binary and normalized versions, respectively; then as the dimension increases so does the classification accuracy, reaching 50% by $r = 15$ and 60%

³In our experiments we used a server with a Intel Xeon W-2195 Skylake 2.3GHz CPU and NIDIA Titan NVIDIA TITAN V VOLTA 12GB GPU.

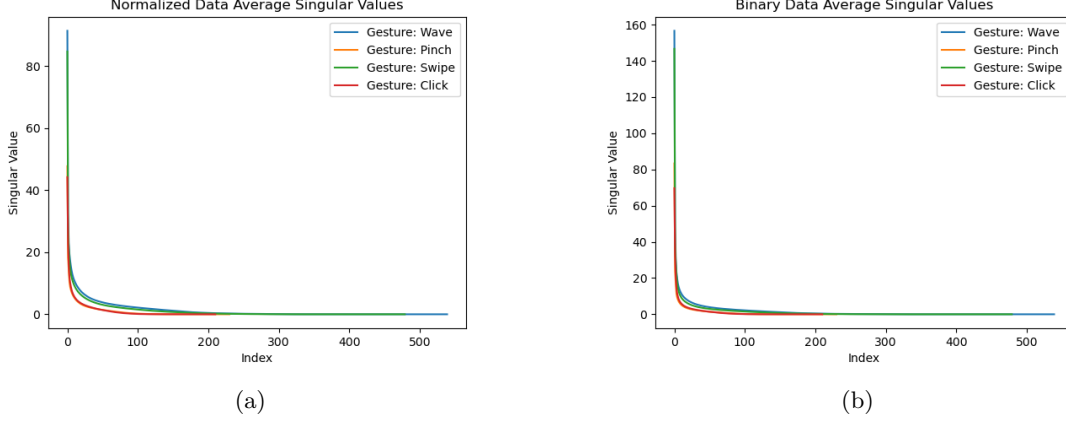


Figure 3: Plot of the average singular values for each gesture. a) Normalized pre-processing is used. b) Binary pre-processing is used.

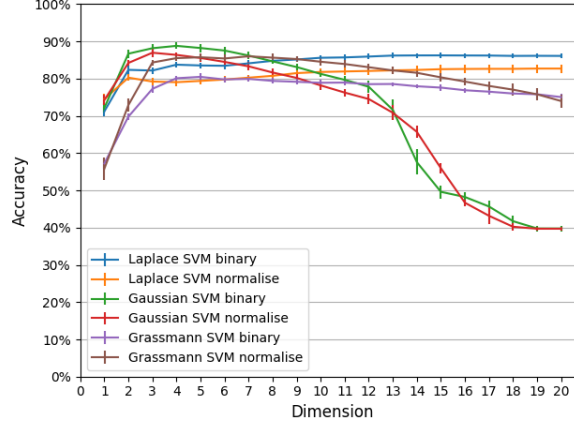


Figure 4: Classification accuracy averaged verse the dimension r of the feature manifold for the five approaches considered.

for $q = 20$. Interestingly, the performance of the Grassman kernel stays constant for $r \in [1, 20]$ with the normalized version maintaining an error of 15% and the binary at 18%. For $r > 9$ the Laplacian kernel obtained roughly the same performance, with the binary feature out performing by 3%, and the Laplacian kernel outperformed the Grassman kernel at larger values of r . We attribute this drop-off in accuracy for increasing r , due to the fact the as dimension of the manifold increases the data points become more spread apart (less dense) and a poorer approximation of the labeling function is achieved.

5.1.5 Robustness to Limited Training Data

In many radio-frequency sensor applications training data is difficult to collect and will likely be the limiting factor of the model's performance. In the case of gesture recognition, not only is cost and effort high, but the data collection involves human subjects [11]. Thus, it is important to develop an approach that is robust to limited data. As a result of the complexity of data collection, what is considered a large data set in micro-Doppler recognition problems will pale in comparison to those used as benchmarks in the Deep Learning community, take for example Image-net used for object recognition [6]. For example, the Dop-net data set consists of 2433 training samples and probably less testing samples⁴.

We evaluate each approach on $\{20, 40, 60, 80\}\%$ of the training data for five trials and average the results. This is done for each of the kernels, hand-crafted features and the CNN, as described in Section 5.1.3. Figure 5 shows

⁴Since the test set is not publicly released, we are assuming the test set is small compared to the training set, which is typical ML practice.

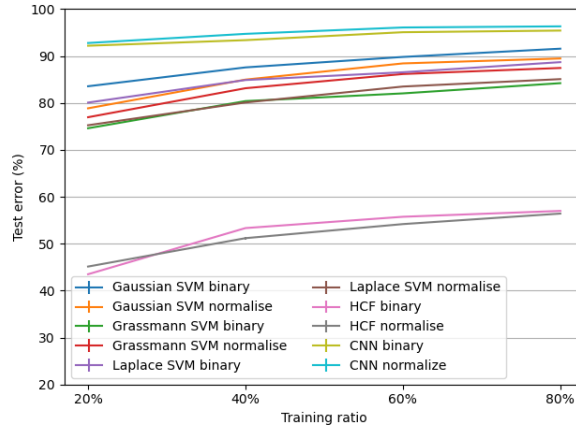


Figure 5: Test error vs. training size for each method and preprocessing approach considered.

the classification accuracy on the reduced training sets. Each combination of kernel and pre-processing technique follow the same trend of increasing test accuracy as the size of the training set increases, as expected. In the case of 10% of the training data, the performance of all methods deteriorates, hand-crafted features and kernel methods degrade by approximately 10%, while surprisingly the CNN is most robust only dropping approximately 5%. In the case of the hand-crafted features and kernel methods this behavior is most likely attributed to the performance of the SVM classifier and not the different feature representation. Furthermore, in the case of the CNN we believe the change in size of the training set is negligible when compared to the degree of over parameterization of the network, making it robust to the small variation. Increasing the size of the training set from 40 – 60% of the original training data, each approach performs similarly, with accuracy dropping approximately only 5%. This behavior continues to 80% of the training data, with the variation in the CNN performance becoming more negligible.

Clearly, the proposed manifold learning approach seems robust to using just a few hundred samples. We attribute this property to a number of factors, first of which is micro-Doppler radar data can be very sensitive to multiple scattering and environmental effects. The choice if pre-processing clearly plays a role in suppressing these nuisance variables, which is then improved by the fact that using only r singular vectors as features further reduces uninformative information.

Furthermore, the r dimensional subspace representation is able to capture the time-varying properties of the data, which are common to a particular class, improving generalization. This is further motivated, by noting that the relationship between the subspace and received radar signals, which span a low-dimensional subspace. To understand this, we observe that in (3.16) the rank of the spectrogram is determined only by the rank of the matrix \mathbf{S} . Therefore, since the micro-Doppler signature consists of a linear combination of delayed and Doppler shifted signals from the dominant scattering points, the rank of the resulting matrix \mathbf{S} is small and captured well using only a small number of singular vectors. Furthermore, the proposed kernel provides good localization at data points on the manifold, which we suspect help to isolate nuisance variables in the data.

It is very surprising that the CNN continues to outperform even with limited training samples, while unsurprisingly, the handcrafted features continue to under-perform. While this may seem impressive, it is difficult to generalize this claim to all micro-Doppler data sets as the literature shows varying performance when used with similar models on different data sets. We think this may be a result of the fact that the training set is already so small to begin with, that the performance when trained on either the full data set or on 20% of it may not make a meaningful difference due to the significantly large over-parameterization of the network. This is in contrast to our kernel approach where the model does not over-parameterize the data. Furthermore, this peculiar performance may also be a result of the pre-processing used prior to input into the CNN. Therefore, further experiments on different and larger data sets would need to be conducted to truly understand the reason and generalization of the CNNs performance, and that is beyond the scope of this paper.

5.1.6 Cross-Subject Generalization

Generalization is an important aspect in any machine learning task and seeks to ensure that the algorithm will perform well on out-of-sample data. In micro-Doppler radar, there are a number of factors that can cause variation of the in- and out-sample distributions, like environmental variations in medium in which the electromagnetic

(EM) wave propagates, changes in material from which the EM waves scatter from, and non-stationary clutter and multiple scattering. For example, in synthetic aperture radar target classification, it has been observed that deep learning classifiers will fail to generalize from synthetic data to measured data. This is attributed to the fact that neural networks tend to learn background surface statistics instead of true features of the object of interest [13]. In this case, the problem is that simulating the scattering off foliage is computationally intractable. These types of challenges have also been observed in classification of communication signals, where algorithms will fail to generalize to data collected on different days.

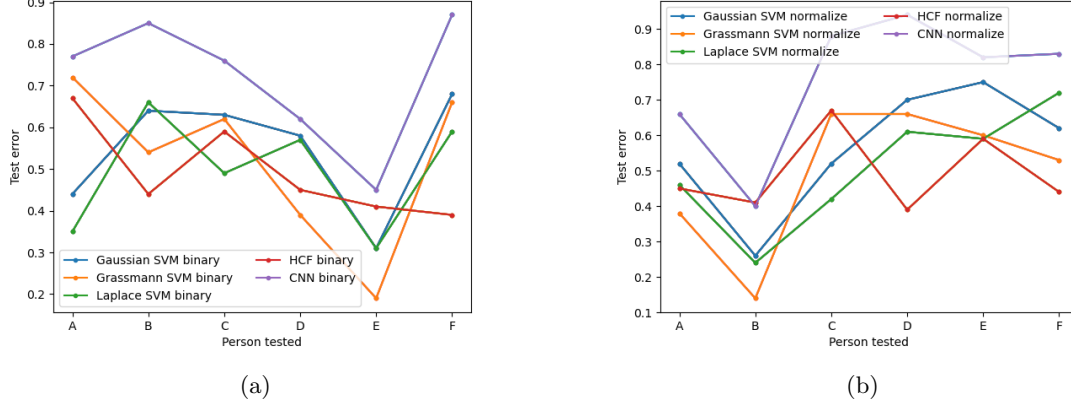


Figure 6: Test accuracy for each algorithm and pre-processing approach when the methods are trained on data from five people and tested on the sixth. a) Normalized pre-processing is used. b) Binary pre-processing is used.

Since the data set consists of collections from six different individuals, it is an interesting question as to whether the manifold learning approach performance is robust to testing on individuals it was not trained on. To investigate this, we train on five of the six individuals and test on the remaining one. We present these results in Figure 6. From these results, it is interesting to see that there is a 40 – 50% variation in performance for each approach when used when data from different persons are held out of the training set. This suggests that there must be characteristics between each person not necessarily captured in the others.

For example, all algorithms perform worst for person E when the data is binary, and on person B when the data is normalized. Since the only variation between these two tests are the pre-processing approach used, this suggests that for classifying gestures of person E, amplitude variation is important in discriminating gestures, because this information is maintained in the normalized data and not in the binary. Furthermore, the converse is true, such that the different approaches perform best on Person E when the data is normalized and worst on person B when it is binary. This suggests that that amplitude information is clearly a nuisance for the classifier. Without additional information on the data collection procedure, which may be meaningful in explaining this phenomena, we suspect this may have to do with a particular persons movement and body size, which can effect the distance of the scattering points to the radar and effect amplitude variation.

Furthermore, general performance trends are positively correlated for persons C, D, and F, when different pre-processing methods are used. These perform with similar accuracy, between 50 – 70%, except for the CNN which typically outperforms by close to 10%. This is consistent with the general trends that we have seen in prior sections. Mainly, the CNN seems to outperform the kernel based methods in both generalization capability and with limited sized training sets. Though, in certain cases, like for binary data, the Grassman kernel appears to perform comparable to the CNN, and in most cases outperform the hand crafted features.

While these results do not provide a clear pattern, it motivates the requirement for a more in depth and controlled study as to what physical effects of the micro-Doppler data are important for achieving good generalization. Thus, we conclude that there is relationship between understanding the data from a physics perspective and what are appropriate algorithms. For example, we have consistently seen the hand crafted features under-perform both the kernel methods and CNN, but in the case of person A binary data and person C normalized data, the handcrafted features outperform the SVD manifold kernels. Overall this suggests that optimal performance is as much a function of the ML algorithm, as it is the data collection approach and pre-processing. An aspect that requires further study, but is left for future work.

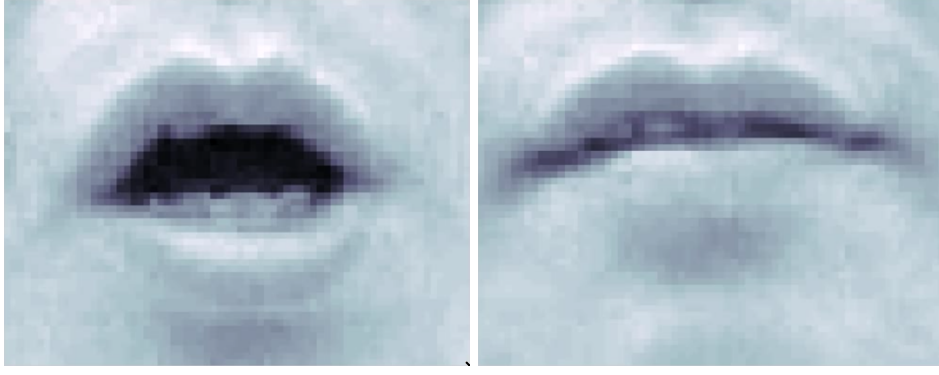


Figure 7: Two example frames from lip video dataset

5.2 Performance on Video-Data

The purpose of this section is demonstrate that our kernel can be used agnostically to the domain knowledge about the data. Toward this goal, we examine a small and simple video data set (without the audio component) where the objective is to identify which digit was spoken in the video. In Section 5.2.1, we describe the data set. Our methodology and results are described in Section 5.2.2.

5.2.1 Data set

We use the data described in [16]. The data consists of video clips of the same person pronouncing digits from 1-5 in English. Each of the five digits is recorded ten times, yielding 50 total videos. Each video is cropped to a 70 x 55 area around the mouth, with the position of the nose held constant, and then converted to grayscale. The problem is to read what digit between one and five the subject is pronouncing in each video clip, effectively a signal classification problem among 5 classes.

5.2.2 Methodology and results

For this dataset, we test the two kernels: the Grassmann kernel as used above as well as a standard radial-basis function kernel on Euclidean space to establish a performance baseline, using a support vector machine to perform classification. Both kernels are defined in Table 2. Each frame of the video clips is flattened into a 3850 x 1 row vector, yielding a 3850 x τ signal for each clip, where τ denotes the number of frames in the clip. For the RBF kernel, we further flatten the signal into a (3850 x τ) x 1 row vector. In accordance to the experiments in [16], the training set consists of 50% data and the test data is the remaining 50%. Specifically, we randomly choose 5 videos from each of the five digit classes to use as training data, totalling 25 videos. We run each test 25 times with randomly-chosen splits each time and average the results below. We compare the performance of our methods to the PCA-EMD algorithm used by Lieu and Saito [16], where the data is transformed into a lower-dimensional representation using principal component analysis, then the earth-mover’s distance is calculated and used for nearest-neighbor classification.

Kernel Type	Expression	Parameters
Grassmann kernel	$\exp(-\gamma(r - \ U_1^T U_2\ _F^2))$	$\gamma = 0.2$
Euclidean kernel	$\exp(-\gamma\ x - x'\ ^2)$	$\gamma = 2.1 \cdot 10^{-7}$

Table 2: The definition of various kernels used for lip video dataset.

The Grassmann kernel performs the best at 96.4% accuracy, outperforming the two methods (PCA-EMD and PCA-HD) originally used on the dataset, as well as the basic Euclidean kernel.

As above, we perform the experiment using differently-sized subsets of training data for the classifiers to evaluate the robustness of each approach to small training sets. Each approach is evaluated on {10, 20, 40, 60, 80}% of the training data for 25 trials each, and each train/test split retains an equal ratio of each class. The results are shown in Figure 9. Similar to the DopNet dataset, performance does not vary significantly within 40-80% training size

Approach	Average Accuracy (%)	Train Time (s)	Test Time (s)
Grassmann SVM	95.84±3.29	3.06±0.39	3.15±0.48
Euclidean SVM	75.20±8.31	2.43±0.28	2.51±0.47
PCA-EMD [16]	94.70		
PCA-HD [16]	90.60		

Figure 8: Classification accuracy of three kernels on lip video dataset

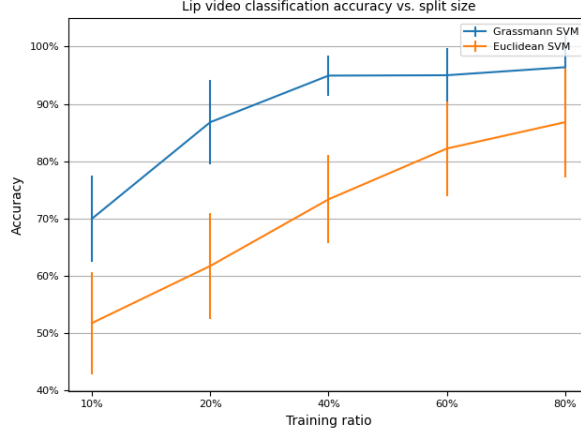


Figure 9: Classification accuracy vs. training size on lip video dataset

using the Grassmann SVM method, suggesting that the Grassmann kernel has strong predictive power with just 20 samples in the training set.

6 Proofs

The proofs of both Theorems 4.1 and 4.2 involves the solution of an interpolation problem. Accordingly, our first objective is to study this problem when Φ_N is an admissible kernel. We assume the set up as in Section 4.

For integer $M \geq 2$, distinct points $y_1, \dots, y_M \in \mathbb{X}$, and real numbers f_1, \dots, f_M , we consider the interpolation problem

$$\sum_{k=1}^M a_k \Phi_N(y_j, y_k) = f_j. \quad (6.1)$$

Our first goal is to investigate when the collocation/normal matrix $[\Phi_N(y_j, y_k)]_{j,k=1}^M$ is invertible and to estimate the norm of this matrix.

Theorem 6.1 *Let $M \geq 2$ be an integer, $\mathcal{C} = \{y_1, \dots, y_M\} \subset \mathbb{X}$, $\eta = \eta(\mathcal{C})$ be defined as in (4.8), $\tilde{\eta} = \min(1, \eta/3)$. We assume that Φ_N is a (q, S) -localized kernel that satisfies (4.6), and further that (4.10) and (4.11) are satisfied. There exists a positive constant C such that if $N \geq C\tilde{\eta}^{-1}$, then the system of equations (6.1) has a solution $\{a_k^*\}$ satisfying*

$$\max_{1 \leq k \leq M} |a_k^*| \lesssim N^{-q} \max_{1 \leq j \leq M} |f_j|, \quad (6.2)$$

and

$$\max_{1 \leq k \leq M} |a_k^* \Phi_N(y_k, y_k) - f_k| \lesssim (N\eta)^{q-S} \max_{1 \leq j \leq M} |f_j|. \quad (6.3)$$

It is convenient to formulate certain technical details of the proof in terms of the notion of a regular measure. If ν is a (positive or signed) measure on \mathbb{X} , we denote by $|\nu|$ its total variation measure. If $d \geq 0$, we say that ν is d -regular if

$$\|\nu\|_d = \sup_{\substack{\mathbf{x} \in \mathbb{X} \\ r > 0}} \frac{|\nu|(\mathbb{B}(\mathbf{x}, r))}{(r + d)^q} < \infty. \quad (6.4)$$

For example, μ^* itself is a 0-regular measure, with $\|\mu^*\|_0$ being the constant involved in (4.10). Another important example is given in the following lemma.

Lemma 6.1 *Let $\mathcal{C} = \{y_1, \dots, y_M\}$ be distinct points in \mathbb{X} , $\eta = \eta(\mathcal{C})$ be as in (4.8), $\tilde{\eta} = \min(1, \eta/3)$, and ν be the counting measure; i.e., the measure that associates the mass 1 with each y_j . Then*

$$\|\nu\|_{\tilde{\eta}} \lesssim \frac{1}{\tilde{\eta}^q}. \quad (6.5)$$

PROOF. Let $x \in \mathbb{X}$, $r > 0$, and J be the number of points in $\mathcal{C} \cap \mathbb{B}(x, r)$. By re-arranging the indices, we may assume without loss of generality that $\mathcal{C} \cap \mathbb{B}(x, r) = \{y_1, \dots, y_J\}$. Then the balls $\mathbb{B}(y_j, \tilde{\eta})$ are pairwise disjoint and the union of these balls is a subset of $\mathbb{B}(x, r + \tilde{\eta})$. Therefore, using the conditions (4.11) and (4.10) on measures of balls, we deduce that

$$J\tilde{\eta}^q \lesssim \sum_{j=1}^J \mu^*(\mathbb{B}(y_j, \tilde{\eta})) \leq \mu^*(\cup_{j=1}^J \mathbb{B}(y_j, \tilde{\eta})) \leq \mu^*(\mathbb{B}(x, r + \tilde{\eta})) \lesssim (r + \tilde{\eta})^q.$$

This implies (6.5). ■

Lemma 6.2 *Let $d \geq 0$ and ν be a d -regular measure. Let Φ_N be a (q, S) -localized kernel. If $N \geq 1$ and $r \geq 1/N$, then*

$$\sup_{x \in \mathbb{X}} \int_{\Delta(x, r)} |\Phi_N(x, y)| d\nu(y) \lesssim \|\nu\|_d (Nr)^{q-S} (1 + d/r)^q. \quad (6.6)$$

Hence,

$$\sup_{x \in \mathbb{X}} \int_{\mathbb{X}} |\Phi_N(x, y)| d\nu(y) \lesssim \|\nu\|_d (1 + Nd)^q, \quad (6.7)$$

and

$$\sup_{x \in \mathbb{X}} \int_{\mathbb{X}} |\Phi_N(x, y)|^2 d\nu(y) \lesssim \|\nu\|_d N^q (1 + Nd)^q \quad (6.8)$$

In particular, taking $d\nu = g d\mu^*$, where $g \in C(\mathbb{X})$, we have $d = 0$, $\|\nu\|_0 \lesssim \|g\|_\infty$, and obtain for $N > 0$

$$\sup_{x \in \mathbb{X}} \int_{\mathbb{X}} |\Phi_N(x, y)| |g(y)| d\mu^*(y) \lesssim \|g\|_\infty. \quad (6.9)$$

PROOF. Without loss of generality, we may replace $|\nu|/\|\nu\|_d$ by ν , and thereby, assume that ν is a positive measure with $\|\nu\|_d = 1$. In this proof only, let $x \in \mathbb{X}$, $A_k = \{y \in \mathbb{X} : 2^k r \leq \rho(x, y) < 2^{k+1} r\}$. Clearly, (6.6) implies that $\nu(A_k) \lesssim 2^{kq} r^q (1 + d/r)^q$. Therefore, using (4.2), we deduce that

$$\begin{aligned} \int_{\Delta(x, r)} |\Phi_N(x, y)| d\nu(y) &= \sum_{k=0}^{\infty} \int_{A_k} |\Phi_N(x, y)| d\nu(y) \\ &\lesssim N^q \sum_{k=0}^{\infty} \int_{A_k} \frac{d\nu(y)}{(N\rho(x, y))^S} \lesssim N^{q-S} r^{-S} \sum_{k=0}^{\infty} 2^{-kS} \int_{A_k} d\nu(y) \\ &\lesssim (Nr)^{q-S} (1 + d/r)^q \sum_{k=0}^{\infty} 2^{-k(S-q)}. \end{aligned}$$

This proves (6.6). To prove (6.7), we observe that

$$\int_{\mathbb{B}(x, 1/N)} |\Phi_N(x, y)| d\nu(y) \lesssim N^q \nu(\mathbb{B}(x, 1/N)) \lesssim N^q (1/N + d)^q = (1 + Nd)^q.$$

The same estimate is obtained for the integral over $\Delta(x, 1/N)$ by using (6.6) with $r = 1/N$. We arrive at (6.7) by adding these estimates. Since (4.2) shows that $|\Phi_N(x, y)| \lesssim N^q$ for all $x, y \in \mathbb{X}$, we get from (6.7) that for any $x \in \mathbb{X}$,

$$\int_{\mathbb{X}} |\Phi_N(x, y)|^2 d\nu(y) \lesssim N^q \int_{\mathbb{X}} |\Phi_N(x, y)| d\nu(y) \lesssim N^q (1 + Nd)^q.$$

■

PROOF OF THEOREM 6.1.

In this proof, we simplify our notation, and write η in place of $\tilde{\eta}$. We consider first the measure ν as in Lemma 6.1, so that with $d = \eta$, $\|\nu\|_d \lesssim \eta^{-q}$. If $N\eta \geq 1$, then we may use (6.6) with $r = \eta$ to obtain

$$\max_{1 \leq k \leq M} \sum_{j \neq k} |\Phi_N(y_j, y_k)| \leq \int_{\Delta(y_j, \eta)} |\Phi_N(y_j, y)| d\nu(y) \lesssim N^q (N\eta)^{-S} (1 + N\eta)^q \lesssim N^q (N\eta)^{q-S}. \quad (6.10)$$

In view of our assumption (4.6), $\Phi_N(y_j, y_j) \gtrsim N^q$. Further, we recall that $S > q$. So, if $N\eta \gtrsim 1$, the matrix $\mathbf{L} = [\Phi_N(y_k, y_k)]_{j,k=1}^M$ satisfies

$$\max_{1 \leq k \leq M} \sum_{j \neq k} |\Phi_N(y_j, y_k)| \leq (1/2) \Phi_N(y_k, y_k), \quad k = 1, \dots, M.$$

The facts that \mathbf{L} is invertible, and (6.2) holds, now follow from well known facts in linear algebra, e.g., [17, Proposition 6.1]. The estimate (6.3) is clear from (6.2) and (6.10). ■

PROOF OF THEOREM 4.1.

Once more, we denote $\tilde{\eta}$ by η . We consider first the case when $\delta(x) \geq \eta/3$. Then using Lemma 6.2 with ν being the measure as in Lemma 6.1, and then using (6.2) we obtain

$$\left| \sum_{k=1}^M a_k^* \Phi_N(x, y_k) \right| \lesssim \|F\|_\infty N^{-q} \sum_{k=1}^M |\Phi_N(x, y_k)| \lesssim \|F\|_\infty N^{-q} \int_{\Delta(x, \eta/3)} |\Phi_N(x, y)| d\nu(y) \lesssim \|F\|_\infty (N\eta)^{-S}. \quad (6.11)$$

Next, we consider the case when $\delta(x) \leq \eta/3$. In this case, there is a unique y_ℓ with $\rho(x, y_\ell) = \delta(x)$, and $y_k \in \Delta(x, \eta/3)$ for all $k \neq \ell$. Arguing as before, we see that

$$\left| a_\ell^* \Phi_n(x, y_\ell) - \sum_{k=1}^M a_k^* \Phi_n(x, y_k) \right| \lesssim \|F\|_\infty (N\eta)^{-S}. \quad (6.12)$$

Therefore, using the Lipschitz conditions (4.7), (6.2), (6.3), we conclude that

$$\begin{aligned} \left| \sum_{k=1}^M a_k^* \Phi_n(x, y_k) - F(x) \right| &\lesssim |a_\ell^* \Phi_n(x, y_\ell) - F(x)| + \|F\|_\infty (N\eta)^{-S} \\ &\leq |a_\ell^* \Phi_n(x, y_\ell) - a_\ell^* \Phi_n(y_\ell, y_\ell)| + |a_\ell^* \Phi_n(y_\ell, y_\ell) - F(y_\ell)| + |F(y_\ell) - F(x)| + \|F\|_\infty (N\eta)^{-S} \\ &\lesssim (N + \|F\|_{\text{Lip}}) \delta(x) + \|F\|_\infty (N\eta)^{q-S}. \end{aligned}$$

■

In order to prove Theorem 4.2, we prove first the following lemmas, which will enable us to apply Theorem 4.1 with $\sigma_N(Ff_0)$ (cf. (4.16)) in place of F and Ψ_N defined in (4.15) in place of Φ_N .

Lemma 6.3 *Let $\{\Phi_N\}$ be a (q, S) -localized family of kernels, and Ψ_N is defined by (4.15). If $d\tau = f_0 d\mu^*$ for some $f_0 \in C(\mathbb{X})$, then $\{\Psi_N\}$ is a (q, S) -localized family of kernels.*

PROOF. In this proof, let $y \neq x \in \mathbb{X}$, and $\delta = \rho(x, y)/3$. Then $\mathbb{B}(x, \delta) \subseteq \Delta(y, \delta)$ and

$$\begin{aligned} |\Psi_N(x, y)| &= \left| \int_{\mathbb{X}} \Phi_N(x, z) \Phi_N(y, z) d\tau(z) \right| \\ &\leq \int_{\Delta(x, \delta)} |\Phi_N(x, z) \Phi_N(y, z)| d\tau(z) + \int_{\mathbb{B}(x, \delta)} |\Phi_N(x, z) \Phi_N(y, z)| d\tau(z) \\ &\leq \int_{\Delta(x, \delta)} |\Phi_N(x, z) \Phi_N(y, z)| d\tau(z) + \int_{\Delta(y, \delta)} |\Phi_N(x, z) \Phi_N(y, z)| d\tau(z). \end{aligned} \quad (6.13)$$

In view of (4.2),

$$|\Phi_N(x, z)| \lesssim \frac{N^q}{\max(1, (N\rho(x, z))^S)} \lesssim \frac{N^q}{\max(1, (N\delta)^S)}, \quad \mathbf{z} \in \Delta(x, \delta). \quad (6.14)$$

The estimates (6.9), (6.14) and (6.13) lead to the fact that Ψ_n is (q, S) -localized.

Next, using (4.2) with $x = y$, we obtain

$$\Psi_N(x, x) = \int_{\mathbb{X}} |\Phi_N(x, z)|^2 d\tau(z) \lesssim N^q \int_{\mathbb{X}} |\Phi_N(x, z)| |f_0(z)| d\mu^*(z).$$

Using (6.9), we deduce that the last integral is $\lesssim \|f_0\|_\infty$. Therefore, $\Psi_N(x, x) \lesssim N^q \|f_0\|_\infty$. ■

Lemma 6.4 *Let $\{\Phi_N\}$ be an admissible family of kernels, and Ψ_N is defined by (4.15). If $d\tau = f_0 d\mu^*$ for some $f_0 \in C(\mathbb{X})$, and $f_0(\mathbf{x}) \geq \mathbf{m}(f_0) > 0$ for $\mathbf{x} \in \mathbb{X}$ then $\{\Psi_N\}$ is an admissible family of kernels.*

PROOF. We have already proved in Lemma 6.3 that $\{\Psi_N\}$ is (q, S) -localized. In order to prove that (4.6) holds with Ψ_N replacing Φ_N , we need only to prove that

$$\Psi_N(x, x) \gtrsim N^q, \quad x \in \mathbb{X}. \quad (6.15)$$

Since Φ_N is admissible, we deduce from (4.7) that there exists $c > 0$ such that if $\rho(x, x') \leq c/N$ then

$$|\Phi_N(x, x) - \Phi_N(x, x')| \lesssim N^{q+1} \rho(x, x') \leq (1/2) |\Phi_N(x, x)|.$$

Using (4.6), we obtain

$$\Psi_N(x, x) = \int_{\mathbb{X}} |\Phi_N(x, z)|^2 f_0(z) d\mu^*(z) \geq \mathbf{m}(f_0) \int_{\mathbb{B}(x, c/N)} |\Phi_N(x, z)|^2 d\mu^*(z) \gtrsim N^{2q} \mathbf{m}(f_0) \mu^*(\mathbb{B}(x, c/N)).$$

In view of (4.11), this leads to (6.15).

Next, if $x, x', y \in \mathbb{X}$, then using (4.7) and (6.9), we obtain

$$|\Psi_N(x, y) - \Psi_N(x', y)| \leq \int_{\mathbb{X}} |\Phi_N(x, z) - \Phi_N(x', z)| |\Phi_N(z, y)| |f_0(z)| d\mu^*(z) \lesssim \|f_0\|_\infty N^{q+1} \rho(x, x').$$

This proves (4.7) with Ψ_N in place of Φ_N . ■

PROOF OF THEOREM 4.2.

Since Ψ_N is an admissible kernel, we may apply Theorem 6.1 with Ψ_N replacing Φ_N and $\sigma_N(Ff_0)(y_j)$ in place of f_j (cf. (4.16)) to obtain $\{a_k^*\}$ such that

$$\sum_{k=1}^M a_k^* \Psi_N(y_k, y_j) = \sigma_N(Ff_0)(y_j) = \int_{\mathbb{X}} \Phi_N(y_j, y) F(y) f_0(y) d\mu^*(y), \quad j = 1, \dots, M, \quad (6.16)$$

and moreover, (cf. (6.2) and (6.3))

$$\max_{1 \leq k \leq M} |a_k^*| \lesssim N^{-q} \max_{1 \leq j \leq M} |\sigma_N(Ff_0)(y_j)|, \quad (6.17)$$

and

$$\max_{1 \leq k \leq M} |a_k^* \Psi_N(y_k, y_k) - \sigma_N(Ff_0)(y_j)| \lesssim (N\eta)^{q-S} \max_{1 \leq j \leq M} |\sigma_N(Ff_0)(y_j)|. \quad (6.18)$$

We note that the minimizer $P_T(\tau; \mathcal{V}(C); F)$ of the theoretical least square loss is given by

$$P_T(\tau; \mathcal{V}(C); F)(x) = \sum_{k=1}^M a_k^* \Phi_N(x, y_k). \quad (6.19)$$

Further, in view of (6.9),

$$\|\sigma_N(Ff_0)\|_\infty \lesssim \|Ff_0\|_\infty. \quad (6.20)$$

Let $x \in \mathbb{X}$ and $\delta(x) > \eta/3$. Then using the measure ν as in Lemma 6.1, we obtain from (6.17), (6.6), and (6.20) that

$$\begin{aligned} |P_T(\tau; \mathcal{V}(C); F)(x)| &\leq \sum_{k: y_k \in \Delta(x, \eta/3)} |a_k^*| |\Phi_N(x, y_k)| \lesssim N^{-q} \|\sigma_N(Ff_0)\|_\infty \int_{y \in \Delta(x, \eta/3)} |\Phi_N(x, y)| d\nu(y) \\ &\lesssim N^{-q} \|\sigma_N(Ff_0)\|_\infty \eta^{-q} (N\eta)^{q-S} \lesssim \|Ff_0\|_\infty (N\eta)^{-S}. \end{aligned} \quad (6.21)$$

This proves (4.18).

Next, let $\delta(x) \leq \eta/3$. Then there exists a unique ℓ such that $\delta(x) = \rho(x, y_\ell)$. So, using the fact that $\Phi_n(y_\ell, y_\ell) \sim \Phi_n(y_\ell, y_\ell) \sim N^q$, (6.18), and (6.20), we obtain

$$\left| a_\ell^* \Phi_n(y_\ell, y_\ell) - \frac{\Phi_n(y_\ell, y_\ell)}{\Psi_n(y_\ell, y_\ell)} \sigma_N(Ff_0)(y_\ell) \right| \lesssim (N\eta)^{q-S} \|\sigma_N(Ff_0)\|_\infty \lesssim (N\eta)^{q-S} \|Ff_0\|_\infty,$$

and hence,

$$\left| a_\ell^* \Phi_n(y_\ell, y_\ell) - \frac{\Phi_n(y_\ell, y_\ell)}{\Psi_n(y_\ell, y_\ell)} F(y_\ell) f_0(y_\ell) \right| \lesssim \|Ff_0 - \sigma_N(Ff_0)\|_\infty + (N\eta)^{q-S} \|Ff_0\|_\infty. \quad (6.22)$$

Since

$$|F(y_\ell) f_0(y_\ell) - F(x) f_0(x)| \leq \|Ff_0\|_{\text{Lip}} \delta(x),$$

we deduce from (6.22), (4.7), (6.17), and (6.20) that

$$\left| a_\ell^* \Phi_n(x, y_\ell) - \frac{\Phi_n(y_\ell, y_\ell)}{\Psi_n(y_\ell, y_\ell)} F(x) f_0(x) \right| \lesssim (N + \|Ff_0\|_{\text{Lip}}) \delta(x) + \|Ff_0 - \sigma_N(Ff_0)\|_\infty + (N\eta)^{q-S} \|Ff_0\|_\infty. \quad (6.23)$$

Arguing as in (6.21), we get

$$\sum_{k \neq \ell} |a_k^* \Phi_n(x, y_k)| \lesssim \|Ff_0\|_\infty (N\eta)^{-S}.$$

Hence, (6.23) leads to (4.19). ■

7 Conclusions

In [18], HNM had developed a very simple method to approximate functions on unknown manifolds without making any effort to learn the manifold itself (e.g., by estimating an atlas or eigen-decomposition of the Laplace-Beltrami operator). This method involves a simple matrix vector multiplication using a specially constructed localized kernel. However, the approach requires that the training data be dense on the manifold. In this paper, we examine the accuracy of the approximation if the training data is sparse instead, and we use either empirical risk minimization or the theoretical square loss minimization. We study this question in a very general setting of a locally compact metric measure space, thereby initializing a theme for further research where the unknown manifold is known to be a sub-manifold of a known manifold rather than just a high dimensional Euclidean space. In practice, the problem arises in analysis of time series, where the domain knowledge indicates that the ambient space is a Grassman manifold. We present a detailed experimental study where we apply a simple case of the kernel to the classification of hand gestures using micro-doppler radar data - a problem of interest in its own right. Our results are comparable with those obtained by the use of CNNs, but with a much shorter training time, and outperform other methods in the literature that use hand-crafted features. To demonstrate the fact that our theory is general purpose, we use similar techniques for the classification of spoken digits from a video data set, and demonstrate how an embedding of the data set onto an unknown submanifold of a Grassman manifold yields superior results.

Acknowledgments

We thank Professor Dr. Naoki Saito at University of California, Davis for providing us with the data set used in [16].

References

- [1] S. Abdulatif, Q. Wei, F. Aziz, B. Kleiner, and U. Schneider. Micro-doppler based human-robot classification using ensemble and deep learning approaches. In *2018 IEEE Radar Conference (RadarConf18)*, pages 1043–1048, 2018.
- [2] S. Ahmed, K. D. Kallu, S. Ahmed, and S. H. Cho. Hand gestures recognition using radar sensors for human-computer-interaction: A review. *Remote Sensing*, 13(3):527, 2021.
- [3] M. Belkin, D. J. Hsu, and P. Mitra. Overfitting or perfect fitting? risk bounds for classification and regression rules that interpolate. In *Advances in Neural Information Processing Systems*, pages 2300–2311, 2018.
- [4] S. Björklund, H. Petersson, and G. Hendeby. Features for micro-doppler based activity classification. *IET radar, sonar & navigation*, 9(9):1181–1187, 2015.
- [5] D. A. Brooks, O. Schwander, F. Barbaresco, J.-Y. Schneider, and M. Cord. Temporal deep learning for drone micro-doppler classification. In *2018 19th International Radar Symposium (IRS)*, pages 1–10, 2018.
- [6] J. Deng, W. Dong, R. Socher, L.-J. Li, K. Li, and L. Fei-Fei. Imagenet: A large-scale hierarchical image database. In *2009 IEEE conference on computer vision and pattern recognition*, pages 248–255. Ieee, 2009.
- [7] F. Filbir and H. N. Mhaskar. A quadrature formula for diffusion polynomials corresponding to a generalized heat kernel. *Journal of Fourier Analysis and Applications*, 16(5):629–657, 2010.
- [8] F. Filbir and H. N. Mhaskar. Marcinkiewicz–Zygmund measures on manifolds. *Journal of Complexity*, 27(6):568–596, 2011.
- [9] W. Gautschi. *Orthogonal polynomials: computation and approximation*. Oxford University Press on Demand, 2004.
- [10] S. Z. Gürbüz, B. Erol, B. Çağhyan, and B. Tekeli. Operational assessment and adaptive selection of micro-doppler features. *IET Radar, Sonar & Navigation*, 9(9):1196–1204, 2015.
- [11] S. Z. Gurbuz and E. Mason. Prologue: Perspectives on deep learning of rf data. In S. Z. Gurbuz, editor, *Deep Neural Network Design for Radar Applications*. IET, 2020.
- [12] A. Huizing, M. Heiligers, B. Dekker, J. de Wit, L. Cifola, and R. Harmanny. Deep learning for classification of mini-uavs using micro-doppler spectrograms in cognitive radar. *IEEE Aerospace and Electronic Systems Magazine*, 34(11):46–56, 2019.
- [13] J. Jo and Y. Bengio. Measuring the tendency of cnns to learn surface statistical regularities. *arXiv preprint arXiv:1711.11561*, 2017.
- [14] C. Karabacak, S. Z. Gurbuz, A. C. Gurbuz, M. B. Guldogan, G. Hendeby, and F. Gustafsson. Knowledge exploitation for human micro-doppler classification. *IEEE Geoscience and Remote Sensing Letters*, 12(10):2125–2129, 2015.
- [15] G. Li, R. Zhang, M. Ritchie, and H. Griffiths. Sparsity-driven micro-doppler feature extraction for dynamic hand gesture recognition. *IEEE Transactions on Aerospace and Electronic Systems*, 54(2):655–665, 2018.
- [16] L. Lieu and N. Saito. Signal Ensemble Classification Using Low-Dimensional Embeddings and Earth Mover’s Distance. In J. Cohen and A. I. Zayed, editors, *Wavelets and Multiscale Analysis: Theory and Applications*, Applied and Numerical Harmonic Analysis, pages 227–256. Birkhäuser, Boston, 2011.
- [17] H. N. Mhaskar. Eignets for function approximation on manifolds. *Applied and Computational Harmonic Analysis*, 29(1):63–87, 2010.
- [18] H. N. Mhaskar. A direct method for function approximation on data defined manifolds. *Neural Networks*, 132:253–268, 2020. ArXiv preprint arXiv:1908.00156, doi:10.1016/j.neunet.2020.08.018.
- [19] H. N. Mhaskar. Kernel-based analysis of massive data. *Frontiers in Applied Mathematics and Statistics*, 6:30, 2020.

- [20] H. N. Mhaskar and T. Poggio. An analysis of training and generalization errors in shallow and deep networks. *Neural Networks*, 121:229–241, 2020.
- [21] P. Molchanov, R. I. Harmanny, J. J. de Wit, K. Egiazarian, and J. Astola. Classification of small uavs and birds by micro-doppler signatures. *International Journal of Microwave and Wireless Technologies*, 6(3-4):435–444, 2014.
- [22] J. Park, R. J. Javier, T. Moon, and Y. Kim. Micro-doppler based classification of human aquatic activities via transfer learning of convolutional neural networks. *Sensors*, 16(12), 2016.
- [23] T. Poggio, K. Kawaguchi, Q. Liao, B. Miranda, L. Rosasco, X. Boix, J. Hidary, and H. Mhaskar. Theory of deep learning III: explaining the non-overfitting puzzle. *arXiv preprint arXiv:1801.00173*, 2017.
- [24] T. Poggio, Q. Liao, B. Miranda, A. Banburski, X. Boix, and J. Hidary. Theory IIb: Generalization in deep networks. *arXiv preprint arXiv:1806.11379*, 2018.
- [25] M. Ritchie, R. Capraru, and F. Fioranelli. Dop-net: a micro-doppler radar data challenge. *Electronics Letters*, 56:568–570(2), May 2020.
- [26] M. S. Seyfioglu, B. Erol, S. Z. Gurbuz, and M. G. Amin. Dnn transfer learning from diversified micro-doppler for motion classification. *IEEE Transactions on Aerospace and Electronic Systems*, 55(5):2164–2180, 2019.
- [27] S. Skaria, A. Al-Hourani, and R. J. Evans. Deep-learning methods for hand-gesture recognition using ultra-wideband radar. *IEEE Access*, 8:203580–203590, 2020.
- [28] G. Szegő. Orthogonal polynomials. In *Colloquium publications/American mathematical society*, volume 23. Providence, 1975.
- [29] D. Tahmoush. Review of micro-doppler signatures. *IET Radar, Sonar & Navigation*, 9(9):1140–1146, 2015.
- [30] K. T. Tran, L. D. Griffin, K. Chetty, and S. Vishwakarma. Transfer learning from audio deep learning models for micro-doppler activity recognition. In *2020 IEEE International Radar Conference (RADAR)*, pages 584–589, 2020.
- [31] P. Turaga, A. Veeraraghavan, A. Srivastava, and R. Chellappa. Statistical computations on grassmann and stiefel manifolds for image and video-based recognition. *Pattern Analysis and Machine Intelligence, IEEE Transactions on*, 33(11):2273–2286, 2011.
- [32] K. Usevich, V. Emiya, D. Brie, and C. Chaux. Characterization of finite signals with low-rank stft. In *2018 IEEE Statistical Signal Processing Workshop (SSP)*, pages 393–397, 2018.
- [33] J.-C. Yen, F.-J. Chang, and S. Chang. A new criterion for automatic multilevel thresholding. *IEEE Transactions on Image Processing*, 4(3):370–378, 1995.
- [34] Z. Zeng, M. G. Amin, and T. Shan. Automatic arm motion recognition based on radar micro-doppler signature envelopes. *IEEE Sensors Journal*, 20(22):13523–13532, 2020.
- [35] C. Zhao, G. Luo, Y. Wang, C. Chen, and Z. Wu. Uav recognition based on micro-doppler dynamic attribute-guided augmentation algorithm. *Remote Sensing*, 13(6), 2021.
- [36] T. Zhou, M. Yang, K. Jiang, H. Wong, and D. Yang. Mmw radar-based technologies in autonomous driving: A review. *Sensors*, 20(24):7283, 2020.
- [37] J. Zhu, H. Chen, and W. Ye. A hybrid cnn-lstm network for the classification of human activities based on micro-doppler radar. *IEEE Access*, 8:24713–24720, 2020.